

Mechanism of Anomalous Anisotropic Colossal Magnetoresistance in Quasi-2D $\text{Mn}_3\text{Si}_2\text{Te}_6$ Bulk Single Crystal

Shiqi Li, Xiong He, Shuai Li, Tianyi Li, Wenhao Zhang, Lizhi Yi, Guangduo Lu, Zhengcai Xia, Yunli Xu,* John Q Xiao,* and Liqing Pan*

$\text{Mn}_3\text{Si}_2\text{Te}_6$, quasi-2D ferrimagnetic semiconductor, exhibits anomalous saturated colossal magnetoresistance (CMR) only when a magnetic field is applied along its magnetic hard magnetization axis, suggesting unconventional underlying physics and promising potential for spintronic applications. However, the intrinsic mechanism behind this anomalous anisotropic CMR remain unresolved. In this work, the temperature and angular dependencies of magnetoresistance (MR) in high-quality $\text{Mn}_3\text{Si}_2\text{Te}_6$ single crystals are systematically investigated. The MR measured within the easy *ab*-plane shows no saturation, whereas a large negative saturation MR of $\approx -100\%$ is observed along the hard magnetization *c*-axis below the Curie temperature. To explain this behavior, a novel model is proposed in which in-plane magnetic fields induce quasi-2D magnetotransport, while out-of-plane fields promote a transition to 3D transport. Notably, when the *c*-axis field exceeds the demagnetizing field, the alignment between spin-polarized carriers and magnetic moments significantly suppresses scattering. The results challenge the applicability of the chiral orbital currents (COC) model in $\text{Mn}_3\text{Si}_2\text{Te}_6$ single crystals and establish a new framework for controlling the CMR effect in layered magnets, offering a pathway toward future spintronic technologies.

1. Introduction

Colossal magnetoresistance (CMR) is a phenomenon observed in certain strongly correlated electron materials, where an applied magnetic field induces a dramatic change in electrical resistance. Since its discovery in perovskite manganites in the 1990s,^[1] CMR has driven extensive research efforts in condensed matter physics and materials science. Materials exhibiting CMR mainly consist of perovskite manganites,^[2–9] bilayer manganites,^[10] oxide spinels,^[11] phosphides,^[12] and certain sulfides.^[13,14] The CMR effect in these materials is governed by strong electronic correlations, with key mechanisms including double-exchange interactions, Jahn-Teller distortions, and charge/orbital ordering.^[2,4,7–9,15–18] Recently, abnormal CMR has been observed in $\text{Mn}_3\text{Si}_2\text{Te}_6$. Different from conventional CMR materials, the $\text{Mn}_3\text{Si}_2\text{Te}_6$ exhibits a distinct behavior: the CMR effect that is prone to saturation only occurs when a magnetic field is applied along the magnetic hard axis, and is

completely unsaturated when the field is aligned with the easy axis-even under full magnetization saturation.^[19–21] This unusual CMR behavior suggests underlying unconventional physics and highlights the materials' promise for future spintronic applications.

$\text{Mn}_3\text{Si}_2\text{Te}_6$ is a quasi-2D ferrimagnetic semiconductor (trigonal, space group $P\bar{3}1c$ (No. 163), $T_C \approx 78$ K) with two inequivalent Mn sites (Mn1 and Mn2) forming a trimer-honeycomb lattice. It exhibits canted ferrimagnetic order, with average magnetic moments of $4.55 \mu_B$ for Mn₁ and $4.20 \mu_B$ for Mn₂.^[22] Recent neutron diffraction results reveal a noncollinear magnetic structure below T_C , where Mn spins are primarily confined to the *ab*-plane but exhibit in-plane canting of 10° toward the *c*-axis under ambient conditions.^[22] Several characteristic properties of $\text{Mn}_3\text{Si}_2\text{Te}_6$ have been identified to date, including anomalous CMR,^[19–21] anisotropic magnetoresistance (AMR),^[19,23] the Nernst effect,^[20] a pressure-induced metal-to-insulator transition,^[24] and the anomalous Hall effect (AHE).^[25,26] Among these, the anomalous CMR effect stands out as particularly striking. Junho Seo et al.^[27] attribute this behavior to a spin orientation-dependent

S. Li, X. He, S. Li, W. Zhang, L. Yi, G. Lu, Y. Xu, L. Pan
Hubei Engineering Research Center of Weak Magnetic-field Detection
College of Science
China Three Gorges University
Yichang 443002, China
E-mail: xuyunli@ctgu.edu.cn; lpn@ctgu.edu.cn

T. Li, Z. Xia
Wuhan National High Magnetic Field Center
Huazhong University of Science and Technology
Wuhan 430074, China

J. Q. Xiao
Department of Physics and Astronomy
University of Delaware
Newark, DE 19716, USA
E-mail: jqx@udel.edu

The ORCID identification number(s) for the author(s) of this article can be found under <https://doi.org/10.1002/advs.202514651>

© 2025 The Author(s). Advanced Science published by Wiley-VCH GmbH. This is an open access article under the terms of the [Creative Commons Attribution](https://creativecommons.org/licenses/by/4.0/) License, which permits use, distribution and reproduction in any medium, provided the original work is properly cited.

DOI: 10.1002/advs.202514651

topological band degeneracy. However, similar to conventional CMR models, this mechanism presumes spin polarization along the c -axis. This raises an intriguing question: how can a small c -axis magnetization component give rise to significant scattering and, consequently, produce such a pronounced CMR effect. Recently, to explain the abnormal CMR effect, the chiral orbital currents (COC)-induced orbital magnetic moments (M_{COC}) model had also been proposed. Their interpretation suggests that the noncollinear magnetic structure of $Mn_3Si_2Te_6$ is crucial for the formation of COC below T_C . These COCs circulate along the edges of $MnTe_6$ octahedra, primarily within the ab -plane, giving rise to a net magnetic moment (M_{COC}) of $\approx 0.1 \mu_B$ predominantly oriented along the c -axis. When a magnetic field is applied along the c -axis, the alignment of M_{COC} also aligns the COCs, reducing scattering significantly and producing the anomalous CMR effect.^[21] The concept of COCs originates from early studies of superconductors, where persistent currents form due to the Meissner effect to expel external magnetic fields. COCs have been investigated in cuprates,^[28–34] iridates,^[35–37] and kagome superconductors.^[38–40] However, in conventional magnetic material systems, identifying comparable mechanism that can generate such circulating currents remains challenging. Therefore, whether the COC model applies to $Mn_3Si_2Te_6$, and whether it fully accounts for the observed anomalous anisotropic CMR, remains an open and compelling question.

In this work, high-quality $Mn_3Si_2Te_6$ single crystals were successfully synthesized, and their magnetic properties, magnetoresistance (MR), and temperature-dependent AMR were characterized systematically. The MR measured with the magnetic field in the easy magnetization ab -plane shows little sign of saturation. While a strong negative MR, reaching $\approx 100\%$, is observed along the hard magnetization c -axis, below the Curie temperature. To understand the origin of this anomalous anisotropic CMR effect, we analyze it in the context of the material's crystal and magnetic structure, offering an alternative perspective to the COC model. Additionally, AMR measurements reveal that the magnetization of $Mn_3Si_2Te_6$ possesses a finite component along the c -axis.

2. Results and Discussion

The crystal structure of $Mn_3Si_2Te_6$ is illustrated in **Figure 1a**. Notably, this compound exhibits a distinctive magnetic configuration characterized by ferromagnetic (FM) order within the ab -plane and antiferromagnetic coupling along the c -axis.^[41] $Mn_3Si_2Te_6$ crystallizes in a layered trigonal structure featuring two inequivalent manganese sites, Mn_1 and Mn_2 . The Mn_1 ions form edge-sharing $MnTe_6$ octahedra, that create a honeycomb lattice within the ab -plane, whereas the Mn_2 ions occupy $MnTe_6$ octahedra arranged in a triangular lattice interleaved between the honeycomb layers. This geometry produces a magnetically frustrated Mn network with three primary antiferromagnetic exchange interactions. The nearest-neighbor interaction (J_1) couples between Mn_1 (honeycomb layer) and Mn_2 (triangular layer) with a bond distance of 3.541(1) Å. The next-nearest-neighbor interaction (J_2) takes place between Mn ions within the basal plane, separated by 4.056(1) Å. A third interaction (J_3) connects Mn ions across adjacent layers at 5.401(1) Å. No structural transition or noticeable anomaly in the lattice constants is observed across the Curie temperature. Both Mn sites exhibit canting of

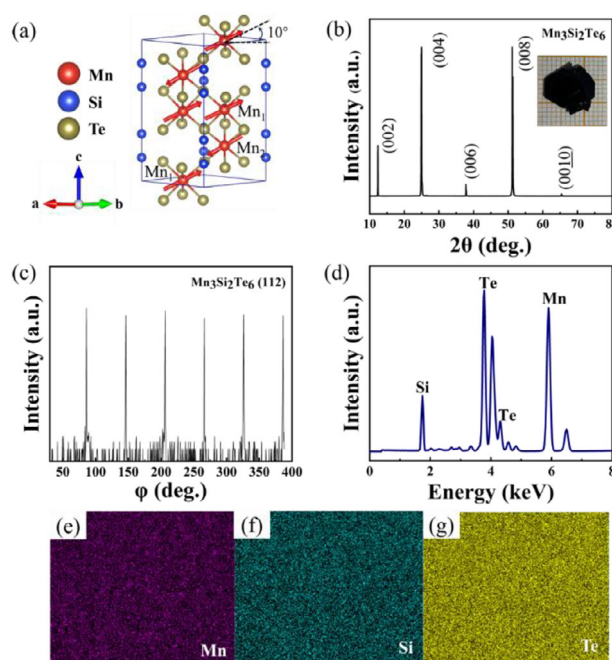


Figure 1. The structure diagram and characterization analysis results of the $Mn_3Si_2Te_6$ single crystal. a) Crystal and magnetic structure of the synthesized $Mn_3Si_2Te_6$. b) Room-temperature XRD spectrum of the $Mn_3Si_2Te_6$ single crystal. The inset is the sample photo. c) ϕ -scan profile demonstrating the crystal's sixfold rotational symmetry. d) EDS spectrum of the $Mn_3Si_2Te_6$. e–g) are the elemental distribution maps.

$\approx 10^\circ$ toward the c -axis.^[22] The XRD diffraction patterns are shown in **Figure 1b**, indicating excellent [001] crystallographic orientation of the synthesized crystals. The crystal quality is further verified with in-plane ϕ -scan (**Figure 1c**), which reveals sixfold symmetry, as expected from trigonal systems. Chemical composition and spatial homogeneity were verified by elemental analysis. Quantitative EDS results (**Figure 1d**) yield an atomic ratio of Mn: Si: Te $\approx 3.0: 1.9: 6.1$, consistent with the ideal stoichiometric ratio of 3:2:6 for $Mn_3Si_2Te_6$. Moreover, elemental mapping (**Figure 1e–g**) demonstrates homogeneous spatial distribution of the Mn, Si, and Te elements throughout the crystal lattice.

Systematic magnetic characterization of $Mn_3Si_2Te_6$ single crystals reveals distinct anisotropic behavior. **Figure 2a,b** presents the temperature-dependent magnetization measured under zero-field-cooled (ZFC) and field-cooled (FC) protocols with applied magnetic fields parallel to the c -axis ($H//c$ -axis) and ab -plane ($H//ab$ -plane), respectively. For $H//c$ -axis, a pronounced bifurcation between the ZFC and FC curves emerges at 78 K (**Figure 2a**), signifying the Curie temperature T_C (78 K). This T_C value is consistent with previous literatures.^[20,41–43] In contrast, for $H//ab$ -plane (**Figure 2b**), the ZFC and FC curves remain superimposed over a broad temperature range due to the ab -plane being the easy magnetization direction, where magnetic moments readily align under external fields. From the Curie-Weiss analysis results on the selected FC data (see **Figure S2**, Supporting Information), the effective magnetic moment of Mn is $4.21 \mu_B$ when H is parallel to the ab -plane, and $3.74 \mu_B$ when H is parallel to the c -axis, respectively. Both values are slightly lower than the neutron diffraction characterization values of 4.2 and $4.5 \mu_B$.^[22]

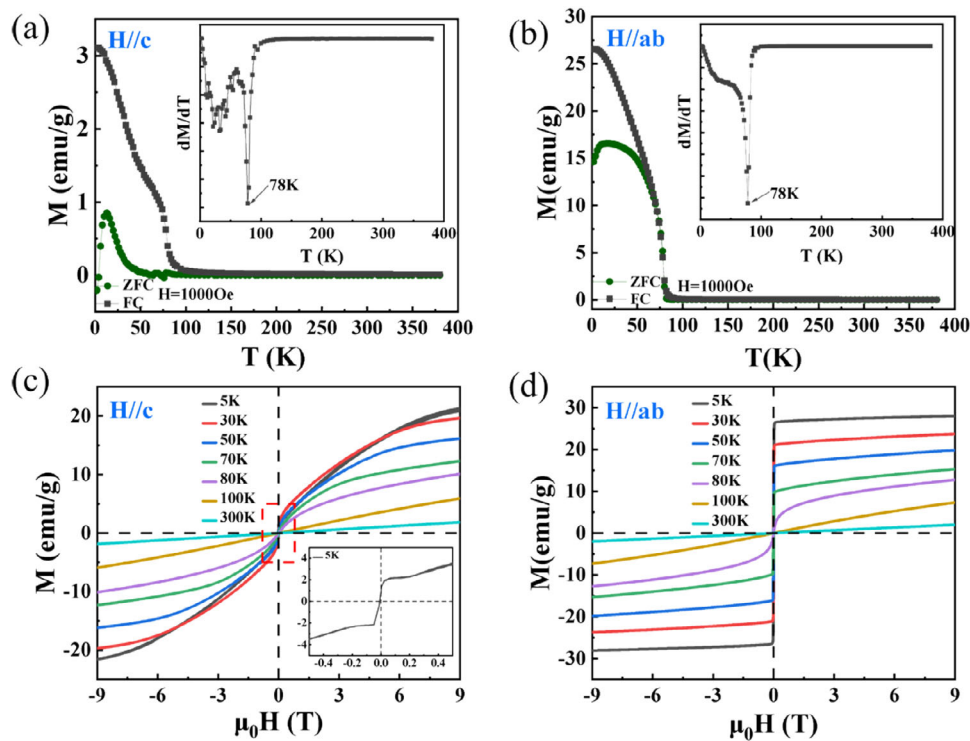


Figure 2. Magnetic properties of the $\text{Mn}_3\text{Si}_2\text{Te}_6$ single crystal. a,b) The temperature-dependent magnetization under zero-field cooling (ZFC) and field cooling (FC) conditions along the $H//c$ -axis and the $H//ab$ -plane, with the field cooling magnetic field being 1000 Oe. Insets: Corresponding derivatives dM/dT . c,d) Magnetic hysteresis (M - H) loops measured at indicated temperatures for (c) $H//c$ -axis and (d) $H//ab$ -plane. The inset in Figure 2c shows an enlarged image at a temperature of 5 K.

Figure 2c,d displays the magnetic hysteresis loops measured at various temperatures with applied fields parallel to the c -axis and ab -plane, respectively. For $H//c$ -axis (Figure 2c), magnetization is not saturated even at the maximum applied field of 9 T. This lack of saturation reveals the strong interlayer antiferromagnetic coupling (J_1). This competitive interplay between the Zeeman energy and the J_1 exchange results in a magnetization process characteristic of ferrimagnetic behavior.^[44] In contrast, for $H//ab$ -plane (Figure 2d), the material exhibits clear easy-axis magnetization below T_c . Saturation magnetization (M_s) increases monotonically with decreasing temperature, consistent with the progressive strengthening of magnetic ordering as thermal fluctuations are suppressed.^[44] Above 100 K, the system shows a fully linear paramagnetic response, confirming that $\text{Mn}_3\text{Si}_2\text{Te}_6$ single crystals transition completely into the paramagnetic state.

The MR properties of the $\text{Mn}_3\text{Si}_2\text{Te}_6$ single crystal are shown in Figure 3. In the case of $H//c$ -axis, when the temperature is 5 K, the resistance of the material changes from ≈ 3600 to 0.5Ω , exhibiting a giant negative MR with strong temperature-dependence (Figure 3a). The MR rapidly drops from 0% to $\approx -100\%$ as the field increases from 0 to 9 T. In contrast, in the case of $H//ab$ -plane, when the temperature is 5 K, the material's resistance varies from ≈ 1700 to 360Ω . The MR in ab -plane remains large and negative but does not saturate even at 9T, as shown in Figure 3b. The negative MR emerges via suppressing the spin fluctuations.^[45] The anisotropic MR behavior is further illustrated in Figure 3c–f, which compare the MR for $H//c$ -axis and $H//ab$ -plane at representative temperatures below the Curie

temperature (5, 30, 50, and 70 K). Notably, the material exhibits an anomalous anisotropic MR: a large saturated negative MR along the magnetically hard magnetization c -axis, in stark contrast to the non-saturating MR along the easy ab -plane. This behavior is opposite to what is typically observed in conventional CMR materials^[7–9] and is consistent with previous reports on $\text{Mn}_3\text{Si}_2\text{Te}_6$.^[19–21]

To elucidate the physical origin of this anomalous anisotropic CMR, we systematically investigate whether the c -axis magnetization component can induce sufficient carrier scattering to account for the observed giant CMR effect. As reported by Ye et al.,^[22] the magnetic moments in the $\text{Mn}_3\text{Si}_2\text{Te}_6$ exhibit a ground-state tilt of 10° from the ab -plane in the absence of an external field. As shown in Figure 4a, applying in-plane magnetic fields does not fully align the Mn spins within the ab -plane, leaving a residual tilt toward the c -axis. This is further supported by the inset of Figure 2c, where a sharp initial increase in magnetization at low fields suggests a pre-existing out-of-plane tilt. As a result, a finite c -axis magnetization component persists (Figure 4a), which leads to strong anisotropic carrier scattering. This spin-dependent scattering mechanism gives rise to the characteristic non-saturating MR observed under $H//ab$ -plane. When the field is applied along the c -axis, increasing field strength progressively tilts spins toward the c -axis, though full saturation is not achieved. Regarding the lattice contribution: when a sufficiently strong external magnetic field, for example along the c -axis, is applied, the spin polarization direction of the conduction electrons becomes aligned with the Mn atomic magnetic moments

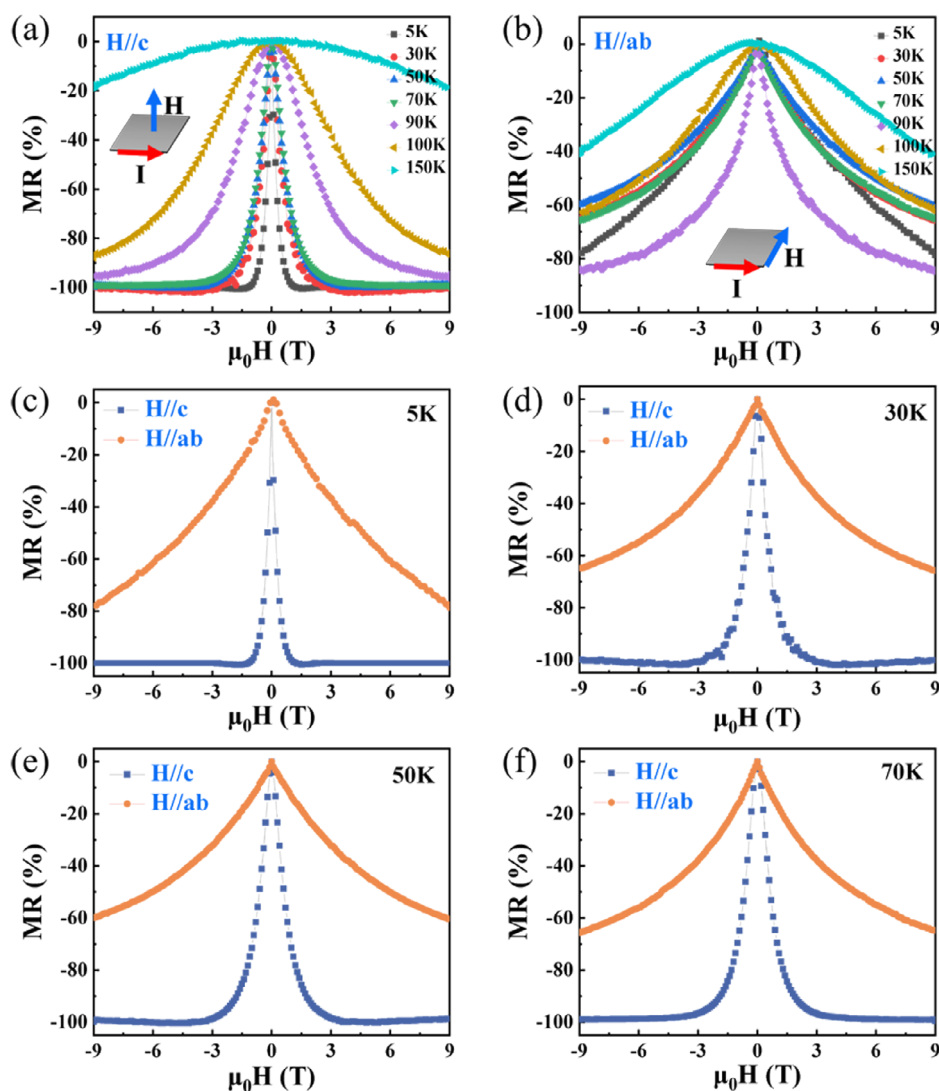


Figure 3. MR properties of the $\text{Mn}_3\text{Si}_2\text{Te}_6$ single crystal. a,b) MR as a function of magnetic field magnitude under different field orientations. c–f) Comparison results of MR perpendicular and parallel to the c -axis at different temperatures.

(Figure 4b). Under this condition, spin-dependent scattering is strongly suppressed, and the residual resistance arises primarily from the lattice scattering. Our measurement results show that the lattice contribution is very small. Therefore, the spin-dependent scattering is the dominant mechanism responsible for the CMR effect in the $\text{Mn}_3\text{Si}_2\text{Te}_6$. To elucidate the mechanism underlying this anisotropic scattering and MR, we further analyze the system with the linear-response theory framework.

The magneto-conductivity can be found from the general Kubo Equation (1),^[46]

$$\sigma_{aa} = \frac{\pi \hbar e^2}{V} \sum_{u,u'} \int \frac{\partial n(\omega)}{\partial \omega} A_u(\omega) A_{u'}(\omega) \left| \langle u' | v_a | u \rangle \right|^2 d\omega \quad (1)$$

where the subscript aa denotes that both the excitation current and the voltage measurement are along a -direction. The effect of the magnetic field is incorporated in the quantum state $|u\rangle$ and $|u'\rangle$, as well as the spectral functions $A_u(\omega)$ and $A_{u'}(\omega)$. Here, V

denotes the volume of the system; $n(\omega)$ is the Fermi-Dirac distribution function, and v_a is the velocity operator along a direction. Given that the Hall signal in $\text{Mn}_3\text{Si}_2\text{Te}_6$ is much smaller than the MR,^[21,26] the magneto-conductivity σ_{aa} is the decisive factor determining the MR.

In Equation (1), the integral over the energy ω and the partial derivative of the Fermi-Dirac distribution function imply the conductivity is mainly contributed by carriers near the Fermi energy when the temperature is not very high. Based on this and the electronic structure of ferrimagnetic $\text{Mn}_3\text{Si}_2\text{Te}_6$ calculated by density functional theory,^[27] one can infer that, the states $|u\rangle$ (also $|u'\rangle$) are from spin-polarized Te- p valence band or Mn- d conduction band.

The spectral function is defined as $A_u(\omega) = i[G_u^R(\omega) - G_u^A(\omega)]/2\pi$, and the retarded and the advanced Green functions are $G_u^R(\omega) = [\omega - \mathcal{H} - \Sigma_u]^{-1}$ and $G_u^A(\omega) = [G_u^R(\omega)]^\dagger$, respectively. Here, \mathcal{H} is the system Hamiltonian. Σ_u is the self-energy of state $|u\rangle$, through which the scattering effect is

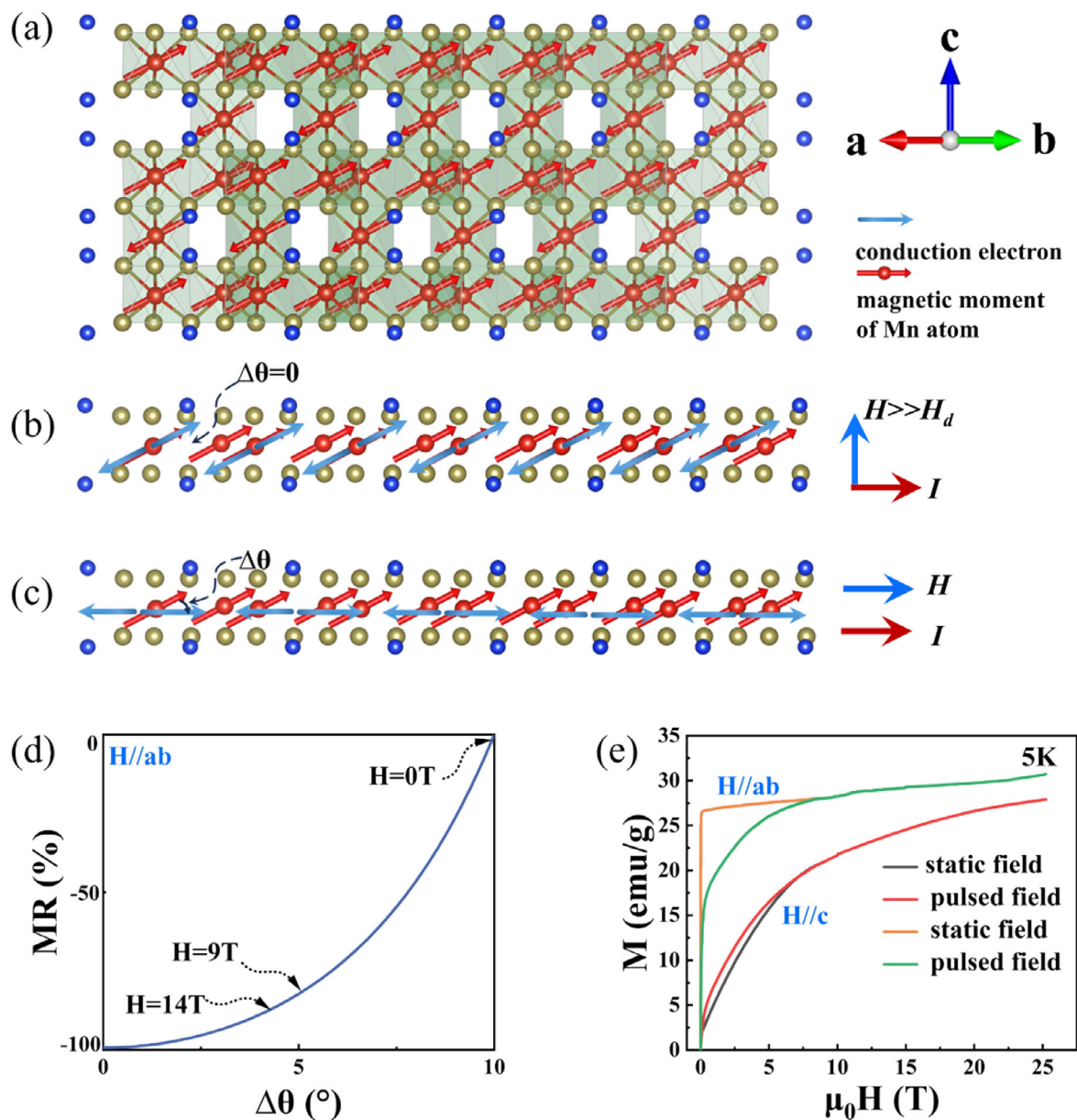


Figure 4. Anomalous anisotropic CMR mechanism diagram and pulsed high magnetic field data. a) Lattice and magnetic ordering of quasi-2D $Mn_3Si_2Te_6$ crystal. b) The situation where the magnetic field is applied along the c -axis. c) The situation where the magnetic field is applied along the ab -plane. [(a) and (b)] The red arrows on the Mn atoms represent the atomic magnetic moments, and the blue arrows represent the polarization direction of the conduction electrons. d) MR as a function of the angle between the direction of carrier spin polarization and Mn magnetic moment. e) High-field magnetization data were collected with the magnetic field applied both parallel ($H//c$ -axis) and perpendicular ($H//ab$ -plane) to the crystallographic c -axis.

considered. The scattering rate is proportional to the imaginary part of the self-energy.^[47] Within the first Born approximation, the self-energy is given by

$$\Sigma_u = \sum_{u'} \frac{|\langle u' | M_{sp} | u \rangle|^2}{\omega - E_{u'} + i\eta} \quad (2)$$

where M_{sp} denotes the general scattering potential, $E_{u'}$ is the energy of state $|u'\rangle$, and η is an infinitesimal positive constant. Since

the spin-dependent scattering dominates in our system, we focus on the spin components in the above formulas. One has

$$|u\rangle \propto \begin{pmatrix} \cos \frac{\theta}{2} \\ e^{i\phi} \sin \frac{\theta}{2} \end{pmatrix} \quad (3)$$

$$M_{sp} \propto \sin \theta' \cos \phi' \sigma_x + \sin \theta' \sin \phi' \sigma_y + \cos \theta' \sigma_z \quad (4)$$

where θ and ϕ denote the spin polarization angles of the carriers, and θ' and ϕ' correspond to the orientations of the local Mn magnetic moments in the $\text{Mn}_3\text{Si}_2\text{Te}_6$.

Under an applied magnetic field, the carriers become uniformly spin polarized. From the scattering matrix in Equation (2), we can define an effective transition amplitude T_i ,

$$T_i = \left| \left(\cos \frac{\theta}{2} \ e^{-i\phi} \sin \frac{\theta}{2} \right) \begin{pmatrix} \cos \theta' & e^{-i\phi'} \sin \theta' \\ e^{i\phi'} \sin \theta' & -\cos \theta' \end{pmatrix} \begin{pmatrix} \cos \frac{\theta}{2} \\ e^{i\phi} \sin \frac{\theta}{2} \end{pmatrix} \right|^2$$

$$= (\cos \theta \cos \theta' + \cos(\phi - \phi') \sin \theta \sin \theta')^2 \quad (5)$$

This effective transition amplitude reaches its maximum value $T_i = 1$ when the spin polarization of carriers aligns with the magnetic moment of Mn atoms, i.e., when $\theta = \theta'$ and $\phi = \phi'$.

In $\text{Mn}_3\text{Si}_2\text{Te}_6$, carriers undergo multiple scattering events during the transport process. The T -matrix approximation for self-energy provides a more accurate descriptions of scattering by including higher-order terms beyond the first Born approximation (proportional to $|\langle u' | M_{sp} | u \rangle|^{2n}$ with $n \geq 2$). This further brings an effective scattering times n for the transition amplitude T_i . By relating magneto-conductivity σ_{aa} to the spectral function, Green function and self-energy, and noting that MR is approximately inversely proportional to σ_{aa} , one has the relation

$$MR = F \left(\frac{1}{T_i^n} \right) \quad (6)$$

where F is a function positively correlated with $\frac{1}{T_i^n}$, and n is the effective number of scattering events.

When a relatively low magnetic field is applied in the ab -plane at 5 K, the magnetization does not reach saturation immediately. A weak field merely rotates the magnetic moments, which initially point in various directions on the easy-magnetization cone, toward positions on the same cone that are closer to the external field. In this regime the moments retain their original tilt of $\approx 10^\circ$ relative to the ab -plane. Thus, $\theta \equiv 0$, due to the quasi-2D nature of the system. Assuming that the scattering potential (Mn magnetic moments) tilts out of the plane by a small angle $\Delta\theta$, i.e., $\theta' = \Delta\theta$, and the azimuthal angles are aligned ($\phi = \phi'$), the MR becomes.

$$MR = F \left(\left(\frac{1}{\cos(\Delta\theta)} \right)^{2n} \right) \propto F \left(\left(1 + \frac{1}{2}(\Delta\theta)^2 \right)^{2n} \right) \quad (7)$$

indicating that even small deviations of Mn moment orientation from the ab -plane can cause appreciable changes in MR.

To estimate $\Delta\theta$ under various field strengths, we model the magnetization response by considering the torque $\vec{L} = \vec{M} \times \vec{B}$ and the work $W = L \cdot \delta$ acting on the magnetic moment. For a system where the exchange interaction between spins s_1 and s_2 is J , the work done by external field is $W = -2J \cdot S^2 \cos\delta$, where δ is the rotation angle of the Mn moment. Balancing these contributions gives $\delta = \frac{BM \sin\varphi}{JS^2}$ where φ is the angle between \vec{B} and \vec{M} . Based on the experimental M - H results and the theoretical saturation magnetization, we obtain $\frac{d\delta}{dB} = 6.357^\circ/\text{T}$. At $\mu_0 H = 9$ T, this gives $\delta = 5.0^\circ$, corresponding to a tilt of 5.0° out of the ab -plane; at 14 T, $\delta = 6.1^\circ$, with a tilt of 3.9° . Assuming $\rho_{\Delta\theta=0^\circ} \ll \rho_{\Delta\theta=10^\circ}$ and

taking $\rho(9\text{T}) \approx 20\% \rho(0\text{T})$, as observed in Figure 4c, we estimate the effective scattering number $n \approx 31$. Using Eqs. (5) and (6), the dependence of MR on the angle between the carrier spin and the Mn moment is plotted in Figure 4d.

As the field strength increases, the magnetic moments gradually overcome the spin-orbit exchange coupling and begin to align with the external field. Because symmetry breaking in this quasi-2D $\text{Mn}_3\text{Si}_2\text{Te}_6$ magnet confines the spin polarization of the conduction electrons strictly to the ab -plane (Figure 4c), there remains a persistent $\sim 5^\circ$ misalignment between the conduction-electron spins and the magnetic moments even at 9 T. This slight misalignment, after multiple scattering events, gives rise to the observed CMR effect.

To further investigate the physical mechanisms underlying the observed MR behavior, we analyze the crystal and magnetic structure of $\text{Mn}_3\text{Si}_2\text{Te}_6$. Given its quasi-2D nature, we model each Mn-containing layer as an infinite 2D slab, a valid approximation for estimating the demagnetizing field. The demagnetizing field is given by: $H_d = N \frac{M}{\mu_0}$, where the demagnetization factor $N = 1$ for an ideal thin plate perpendicular to the applied field. Using the per-Mn magnetic moment $4.5 \mu_B$, as determined by neutron diffraction,^[22] we estimate the maximum demagnetizing field H_d for a single Mn atom to be as high as 1.6 T. When the magnetic moment is tilted 10° from the ab -plane, the remanent magnetic field is 0.28 T, placing the effective retreating field range between 0.28 and 1.6 T.

For out-of-plane ($H//c$ -axis) magnetic fields below this demagnetizing field, the spin polarization remains predominantly in the ab -plane. However, once the external field substantially exceeds the demagnetization field of the quasi-2D $\text{Mn}_3\text{Si}_2\text{Te}_6$, the electron spins reorient toward the direction of the Mn atomic magnetic moments, no longer constrained by the strong in-plane spin limitation characteristic of quasi-2D transport (Figure 4b), maximizing the transition amplitude $T_i = 1$. Consequently, the resistivity ρ_H at $H \gg H_d$ becomes much lower than its zero-field value, leading to an MR near -100% . Magnetization measurements along the c -axis show a continuous increase with applied field strength. According to the circulating orbital current (COC) model proposed by Zhang et al.,^[21] an additional magnetic contribution M_{COC} could enhance the total magnetization. If this model were applicable to $\text{Mn}_3\text{Si}_2\text{Te}_6$, the maximum magnetization would equal the theoretical saturation plus the COC contribution. Given that the reported circulating current per unit cell is 10, with each current contributing $0.1 \mu_B$, the calculated maximum magnetization would reach $\approx 30 \text{ emu g}^{-1}$. However, our high-field data (Figure 4e) show that the measured values for $H//c$ remain well below this theoretical limit. Additionally, the magnetization along $H//c$ is significantly smaller than that observed along $H//ab$ (Figure 4e). Very recently, no definitive evidence of the M_{COC} is observed in Fang et al.' study.^[48] Meanwhile, Joule heating effects may also contribute to the anomalous CMR effect.^[42,48] Based on the above analysis, we believe that the COC model does not adequately describe $\text{Mn}_3\text{Si}_2\text{Te}_6$ single crystals.

In addition, as shown in Figure S1 (Supporting Information), the trigonal crystal structure of $\text{Mn}_3\text{Si}_2\text{Te}_6$ features non-collinear Mn-Te-Mn bonds and a honeycomb arrangement of MnO_6 octahedra-distinct from the corner-sharing MnO_6 octahedra found on perovskite manganites. Consequently, the CMR mechanism differs from both the conventional double-exchange

and Jahn-Teller distortion models.^[8,9] Apart from the double-exchange and Jahn-Teller distortion, the electronic phase separation mechanism is most experimentally supported in the perovskite manganites system.^[7] In that scenario the antiferromagnetic charge-ordered insulating phase competes with the ferromagnetic metallic phase; under an applied magnetic field the system transitions to the ferromagnetic metallic state, producing a characteristic inflection in the magnetization (M - H) curve.^[7] In our $\text{Mn}_3\text{Si}_2\text{Te}_6$ crystals, no such transition is observed (Figure 2c,d). The M - H curves show only a low-field inflection that arises from the reorientation of the magnetic moment along different easy axes. Under a weak field, the moment initially aligns along the in-plane directions closest to the field, and with increasing field they gradually rotates toward the field direction until saturation. This low-field feature is not related to any magnetic phase transition, and the MR curves show no corresponding anomaly in this region. Even at higher fields no additional inflection points appear. Moreover, electronic phase separation in perovskite manganites requires charge ordering arising from mixed valence states such as $\text{Mn}^{+3}/\text{Mn}^{+4}$ or $\text{Fe}^{+2}/\text{Fe}^{+3}$.^[8,9] In contrast, Mn ions in $\text{Mn}_3\text{Si}_2\text{Te}_6$ retain a stable +2 valence,^[49,50] which rules out the formation of charge-ordered phase. Therefore, the CMR mechanism in $\text{Mn}_3\text{Si}_2\text{Te}_6$ differs fundamentally from all three conventional models. Bases on our detailed theoretical analysis, we conclude that electron-correlation-driven spin-dependent scattering is the dominant origin of the anomalous anisotropic CMR in this $\text{Mn}_3\text{Si}_2\text{Te}_6$ materials.

To further verify the presence of a finite magnetization component along the c -axis, we performed angular-dependent anisotropic magnetoresistance (AMR) measurements (Figure 5). The magnetic field was applied in three principal planes (yz , xz , and xy), labeled as rotation angle α , β , and γ , respectively (Figure 5a,d,g). Herein, the x , y , and z axes correspond to the [010], [210], and [001] crystallographic directions, respectively. Figure 5b,c displays the angular dependence of the AMR measured in the yz plane under various constant magnetic fields, revealing clear twofold symmetry. The AMR amplitude gradually diminishes with increasing temperature. The angular dependence can be empirically described by:^[51]

$$\text{AMR} = \left(\frac{R_{xx,\theta} - R_{xx,0}}{R_{xx,0}} \right) \times 100\% \quad (8)$$

where $R_{xx,\theta}$ is the longitudinal resistance at angle θ , and $R_{xx,0}$ is the resistance at $\theta = 0$.

Figure 5e,f depicts the angular dependence of the AMR within the xz plane, which shows weaker anisotropy compared to the yz plane, although a similar temperature dependence is observed. In contrast, AMR in the xy plane (Figure 5h,i) exhibits minimal variation, indicating that, MR within the ab -plane is largely insensitive to the in-plane orientation of the magnetic field relative to the current. This result reinforces the conclusion that the dominant spin orientation lies near the ab -plane with a measurable tilt toward the c -axis.

Although $\text{Mn}_3\text{Si}_2\text{Te}_6$ has threefold crystallographic symmetry about the c -axis, its easy magnetization direction lies on a conical surface tilted $\approx 80^\circ$ from this axis. This configuration exhibits in-plane isotropy (e.g., $\text{AMR}_{xy} \approx 0$) around the c -axis and effectively breaks the original threefold rotation symmetry, giving rise in-

stead to a fourfold symmetric AMR. The angular dependence of the MR is well-described by the empirical formula, where ψ_{AMR} and φ_{AMR} denote the angles between the magnetization and the current direction, and between the magnetization and the [100] crystallographic axis, respectively.^[51]

$$\text{AMR} = C_1 \cos 2\varphi_{AMR} + C_2 \cos 2\psi_{AMR} + C_4 \cos 4\psi_{AMR} + C_{IC} \cos (4\psi_{AMR} - 2\varphi_{AMR}) \quad (9)$$

where the C_1 , C_2 , C_4 , and C_{IC} are phenomenological coefficients representing the noncrystalline term, twofold and fourfold crystalline terms, and a mixed crystalline/noncrystalline term, respectively.

For simplicity, the AMR signal is fitted using the expression:

$$C_2 \cos \left(2(\theta_{AMR} + \varphi_S) \times \frac{3.14}{180} \right) + mC_4 \cos \left(4 \times (\theta_{AMR} + \varphi_S) \times \frac{3.14}{180} \right) + A \quad (10)$$

where θ_{AMR} is the rotation angle and φ_S is a phase offset angle relative to the symmetry axes nominally at 90° and 270° . As temperature increases, C_2 increases steadily (Figure 6a,d), while the fourfold coefficient C_4 decreases (Figure 6b,e). The twofold symmetry dominates the AMR signal, and more so at higher temperatures. The microscopic origin of such fourfold symmetric AMR remains an active research topic.^[52-54] Considering that $\text{Mn}_3\text{Si}_2\text{Te}_6$ crystallizes in a structure analogous to Bismuth and MnBi_2Te_4 ^[53] and exhibits half-metallicity,^[25] the observed unusual fourfold AMR most likely originates from the topological orbital moment of magnetic Bloch electrons,^[53] rather than from relaxation time anisotropy^[52] or high-order term of spin-orbit interactions^[54] in a cubic system. Furthermore, the phase offset parameter φ_S reveals peak shift of $\approx 5^\circ$ in the β -plane and 3.6° in the α -plane, respectively (Figure 6c,f), suggesting that the MR maxima occur when the strong magnetic field is rotated $\approx 3^\circ$ to 5° beyond the principle symmetry axes (90° and 180°). These shifts provide further evidence that the magnetic moments in the $\text{Mn}_3\text{Si}_2\text{Te}_6$ are tilted with respect to the ab -plane.

3. Conclusion

High-quality $\text{Mn}_3\text{Si}_2\text{Te}_6$ single crystals were synthesized via the solvent-flux method. Magnetic characterization revealed that the magnetization along the easy axis within the ab -plane did not fully saturate, and that the material exhibits anomalous MR in the ferrimagnetic state. Specifically, when a magnetic field was applied along the hard magnetization c -axis, $\text{Mn}_3\text{Si}_2\text{Te}_6$ exhibited behaves consistent with a conventional 3D ferrimagnet. Once the demagnetizing field was overcome, the alignment of spin polarization with the magnetic moments suppressed spin-disorder scattering, resulting in a large negative saturation MR. Conversely, for in-plane magnetic fields, the MR remained unsaturated, attributed to persistent spin misalignment caused by a c -axis component of the magnetization. AMR measurements further revealed distinct angular evolution patterns under in-plane versus out-of-plane fields, consistent with a quasi-2D transport character and tilted spin structure. Our findings not only deviate

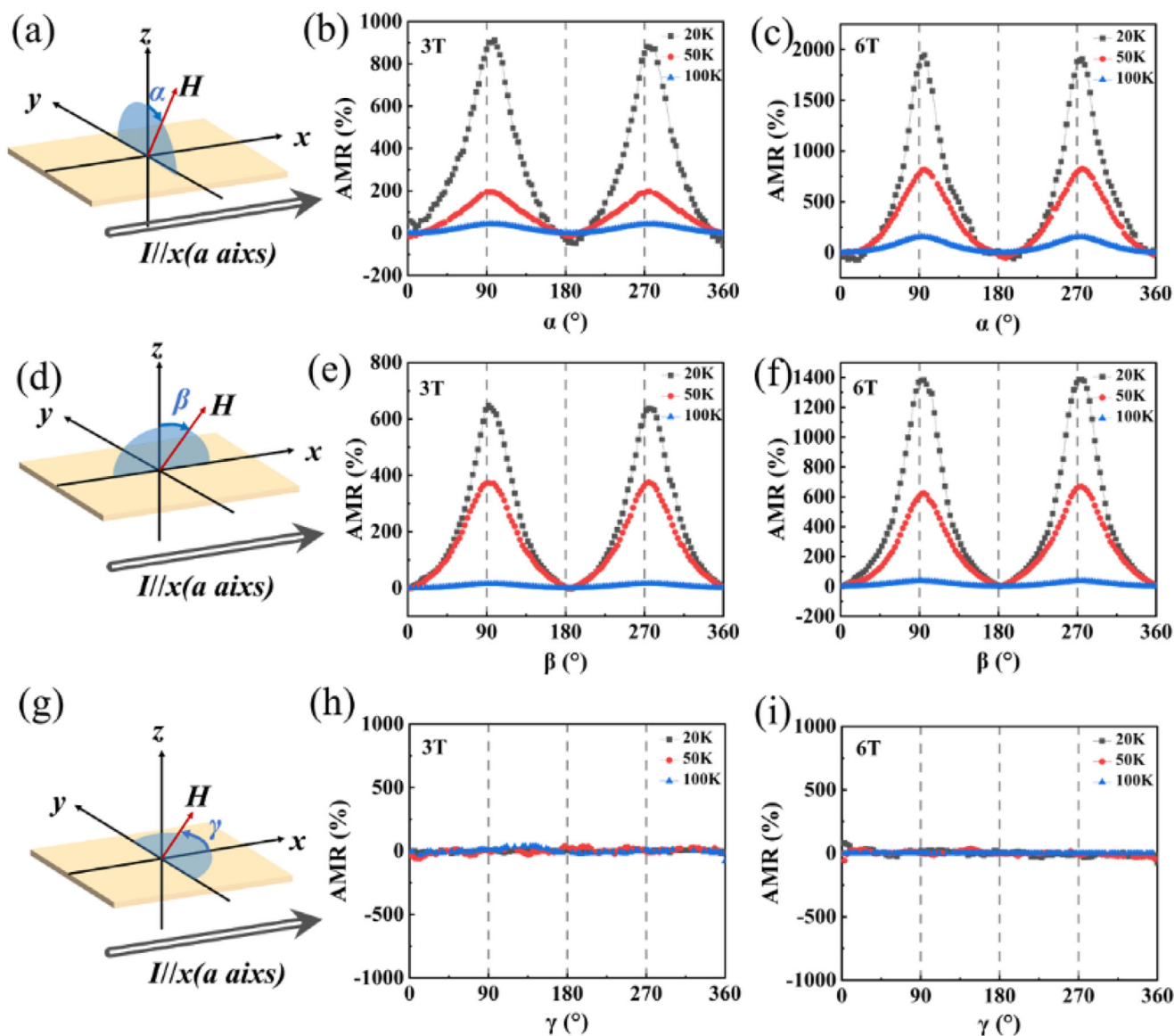


Figure 5. The AMR properties of the $\text{Mn}_3\text{Si}_2\text{Te}_6$ single crystal. a) Schematic diagram illustrating the AMR measurement configuration in the yz -plane. b,c) Angle-dependent AMR data measured at magnetic fields of 3 T and 6 T, respectively. d) Schematic diagram illustrating the AMR measurement configuration in the xz -plane. e,f) Angle-dependent AMR results measured at 3 and 6 T, respectively. g) Schematic diagram illustrating the AMR measurement configuration in the xy -plane. h,i) Angle-dependent AMR data measured at magnetic fields of 3 and 6 T, respectively.

from traditional frameworks based on double exchange or Jahn-Teller distortions mechanisms, but also challenge the applicability of the COC model in $\text{Mn}_3\text{Si}_2\text{Te}_6$ single crystals system. The results, establish a new framework for manipulating magneto-transport in layered magnets. This study advances the fundamental understanding of the anomalous anisotropic CMR effect in $\text{Mn}_3\text{Si}_2\text{Te}_6$ and highlights its potential for future spintronic applications.

4. Experimental Section

High-purity single crystals were synthesized employing an improved self-flux growth methodology. Stoichiometric amounts of high-purity Mn (99.99%), Si (99.999%), and Te (99.999%) were precisely weighed in a mo-

lar ratio of 3:2:12 and sealed in an alumina crucible. The crucible was then sealed within a quartz tube under a high vacuum of 10^{-5} Pa. The sample was heated to 1000 °C at a rate of 100 °C h^{-1} , held for 24 h to ensure complete melting and homogenization in a muffle furnace. Subsequently, the sample was cooled at 2 °C h^{-1} from 1000 to 700 °C over 150 h to promote crystal nucleation and directional growth. The crucible was quickly removed from the furnace, and the flux was separated from the crystals by centrifugation, yielding well-defined hexagonal plate-like single crystals up to centimeter-sized as shown in the inset of Figure 1a.

The sample structure was characterized using powder X-ray diffraction (XRD, Rigaku SmartLab) equipped with $\text{Cu-K}\alpha$ radiation. Elemental distribution analysis was conducted via scanning electron microscopy (SEM, JEOL JSM-7500F) coupled with energy-dispersive X-ray spectroscopy (EDS). To investigate the magnetic and electrical transport properties of $\text{Mn}_3\text{Si}_2\text{Te}_6$, comprehensive characterization was carried out using a physical property measurement system (PPMS DynaCool, 9T, Quantum De-

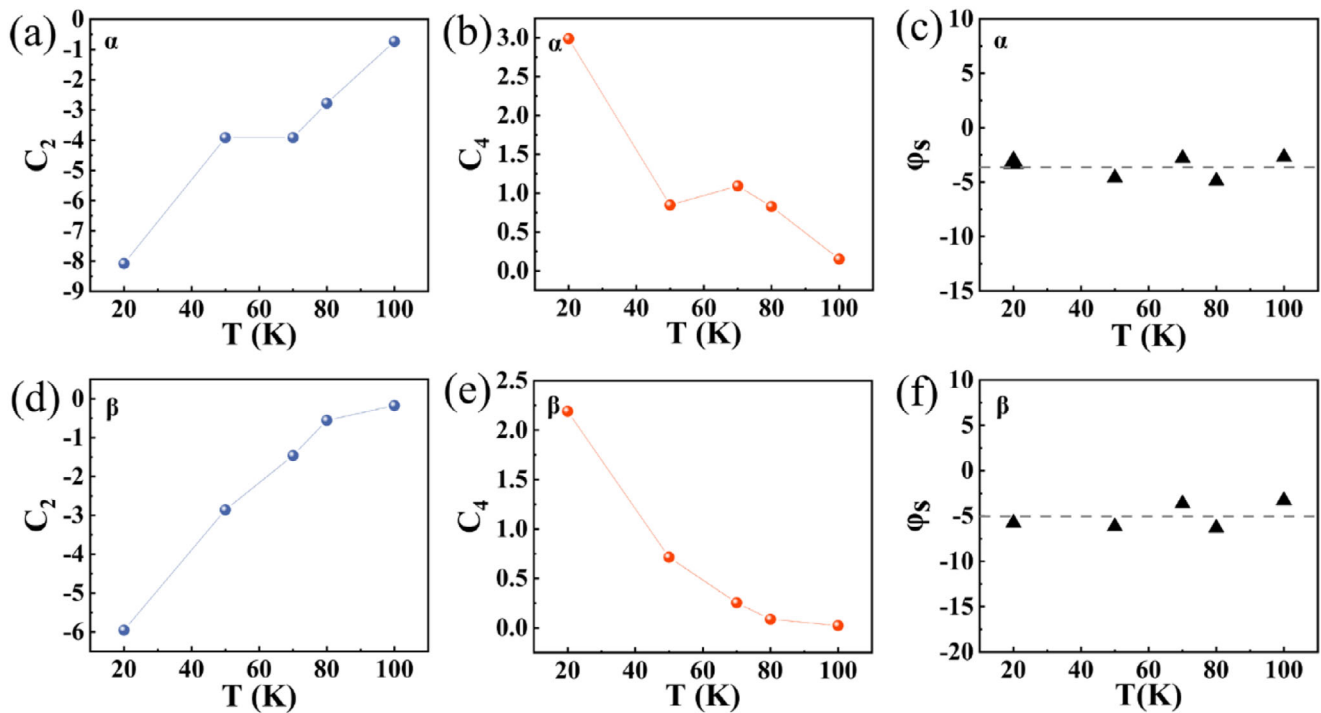


Figure 6. The fitting parameters obtained based on the AMR results at different temperatures. a–c) show the fitted AMR data for the α -plane. d–f) present the fitted parameters for the β -plane.

sign). The MR measurements were performed employing the standard four-point method. Magnetization measurements were performed using a vibrating sample magnetometer in a Physical Property Measurement System (PPMS-14T, Quantum Design) with fields applied both parallel to the ab -plane and along the c -axis. High-magnetic-field measurements were conducted at the Wuhan National High Magnetic Field Center. The Zero-Field Cooled (ZFC) and Field Cooled (FC) magnetization curves of a $\text{Mn}_3\text{Si}_2\text{Te}_6$ single crystal were measured over a temperature range of 2–380 K. For the ZFC protocol, the sample was first cooled from 380 to 2 K in the absence of an external magnetic field. A probe field of 100 Oe was then applied, and the magnetization was recorded while warming the sample to 380 K. For the FC curve, the sample was cooled from 380 to 2 K under a static magnetic field of 1000 Oe, and the magnetization was subsequently measured during the warming cycle from 2 to 380 K under the same field.

Data Availability Statement

The data that support the findings of this study are available from the corresponding author upon reasonable request.

Keywords

anisotropic magnetoresistance, anomalous magnetotransport, colossal magnetoresistance, quasi-2D magnetic material, spin-dependent scattering

Received: August 1, 2025
Revised: September 18, 2025
Published online:

Supporting Information

Supporting Information is available from the Wiley Online Library or from the author.

Acknowledgements

S.L., X.H., and S.L. contributed equally to this work. This work was supported in part by the National Natural Science Foundation of China (Grant Nos. 12274258, 12504059), the Natural Science Foundation of Hubei Province (Grant Nos. 2024AFB333, 2024AFB289), and the Natural Science Foundation of Yichang (Grant No. A24-3-021).

Conflict of Interest

The authors declare no conflict of interest.

- [1] A. Goyal, M. Rajeswari, R. Shreekala, S. E. Lofland, S. M. Bhagat, T. Boettcher, C. Kwon, R. Ramesh, T. Venkatesan, *Appl. Phys. Lett.* **1997**, *71*, 2535.
- [2] J. Fontcuberta, B. Martínez, A. Seffar, S. Piñol, J. L. García-Muñoz, X. Obradors, *Phys. Rev. Lett.* **1996**, *76*, 1122.
- [3] E. L. Nagaev, *Phys. Rep.* **2001**, *346*, 387.
- [4] A. Ramirez, *J. Phys.: Condens. Matter* **1997**, *9*, 8171.
- [5] K. H. Ahn, X. W. Wu, K. Liu, C. L. Chien, *Phys. Rev. B* **1996**, *54*, 15299.
- [6] H. Röder, J. Zang, A. R. Bishop, *Phys. Rev. Lett.* **1996**, *76*, 1356.
- [7] D. Saurel, A. Brûlet, A. Heinemann, C. Martin, S. Mercone, C. Simon, *Phys. Rev. B* **2006**, *73*, 094438.
- [8] K. H. Hong, A. M. Arevalo-Lopez, J. Cumby, C. Ritter, J. P. Attfield, *Nat. Commun.* **2018**, *9*, 2975.
- [9] Y.-K. Liu, Y.-W. Yin, X.-G. Li, *Chin. Phys. B* **2013**, *22*, 087502.
- [10] D. N. Argyriou, J. F. Mitchell, P. G. Radaelli, H. N. Bordallo, D. E. Cox, M. Medarde, J. D. Jorgensen, *Phys. Rev. B* **1999**, *59*, 8695.

- [11] J. Philip, T. Kutty, *Mater. Lett.* **1999**, *39*, 311.
- [12] Z.-C. Wang, J. D. Rogers, X. Yao, R. Nichols, K. Atay, B. Xu, J. Franklin, I. Sochnikov, P. J. Ryan, D. Haskel, F. Tafti, *Adv. Mater.* **2021**, *33*, 2005755.
- [13] S. Weber, P. Lunkenheimer, R. Fichtl, J. Hemberger, V. Tsurkan, A. Loidl, *Phys. Rev. Lett.* **2006**, *96*, 157202.
- [14] O. Lang, C. Felser, R. Seshadri, F. Renz, J.-M. Kiat, J. Ensling, P. Gütllich, W. Tremel, *Adv. Mater.* **2000**, *12*, 65.
- [15] Y. Sun, W. Tong, X. Xu, Y. Zhang, *Phys. Rev. B* **2001**, *63*, 174438.
- [16] M. Sturge, *Solid State Physics*, 1st ed., Academic Press, New York City **1968**.
- [17] R. G. Pearson, *Proc. Natl. Acad. Sci. USA* **1975**, *72*, 2104.
- [18] C. Zener, *Phys. Rev.* **1951**, *82*, 403.
- [19] Y. Ni, H. Zhao, Y. Zhang, B. Hu, I. Kimchi, G. Cao, *Phys. Rev. B* **2021**, *103*, L161105.
- [20] C. Ran, X. Mi, J. Shen, H. Wang, K. Yang, Y. Liu, G. Wang, G. Wang, Y. Shi, A. Wang, Y. Chai, X. Yang, M. He, X. Tong, X. Zhou, *Phys. Rev. B* **2023**, *108*, 125103.
- [21] Y. Zhang, Y. Ni, H. Zhao, S. Hakani, F. Ye, L. DeLong, I. Kimchi, G. Cao, *Nature* **2022**, *611*, 467.
- [22] F. Ye, M. Matsuda, Z. Morgan, T. Sherline, Y. Ni, H. Zhao, G. Cao, *Phys. Rev. B* **2022**, *106*, L180402.
- [23] C. Huang, M. Huo, X. Huang, H. Liu, L. Li, Z. Zhang, Z. Chen, Y. Han, L. Chen, F. Liang, H. Dong, B. Shen, H. Sun, M. Wang, *Phys. Rev. B* **2024**, *109*, 205145.
- [24] R. A. Susilo, C. I. Kwon, Y. Lee, N. P. Salke, C. De, J. Seo, B. Kang, R. J. Hemley, P. Dalladay-Simpson, Z. Wang, D. Y. Kim, K. Kim, S.-W. Cheong, H. W. Yeom, K. H. Kim, J. S. Kim, *Nat. Commun.* **2024**, *15*, 3998.
- [25] D. Li, M. Wang, D. Li, J. Zhou, *Phys. Rev. B* **2024**, *109*, 155153.
- [26] Y. Zhang, Y. Ni, P. Schlottmann, R. Nandkishore, L. E. DeLong, G. Cao, *Nat. Commun.* **2024**, *15*, 3579.
- [27] J. Seo, C. De, H. Ha, J. E. Lee, S. Park, J. Park, Y. Skourski, E. S. Choi, B. Kim, G. Y. Cho, H. W. Yeom, S.-W. Cheong, J. H. Kim, B.-J. Yang, K. Kim, J. S. Kim, *Nature* **2021**, *599*, 576.
- [28] C. M. Varma, *Phys. Rev. B* **2006**, *73*, 155113.
- [29] C. M. Varma, *J. Phys.: Condens. Matter* **2014**, *26*, 505701.
- [30] S. S. Pershoguba, K. Kechedzhi, V. M. Yakovenko, *Phys. Rev. Lett.* **2013**, *111*, 047005.
- [31] V. Scagnoli, U. Staub, Y. Bodenthin, R. A. de Souza, M. García-Fernández, M. Garganourakis, A. T. Boothroyd, D. Prabhakaran, S. W. Lovesey, *Science* **2011**, *332*, 696.
- [32] S. Di Matteo, M. R. Norman, *Phys. Rev. B* **2012**, *85*, 235143.
- [33] V. M. Yakovenko, *Phys. B* **2015**, *460*, 159.
- [34] P. Bourges, D. Bounoua, Y. Sidis, *C. R. Phys.* **2021**, *22*, 7.
- [35] J. Jeong, Y. Sidis, A. Louat, V. Brouet, P. Bourges, *Nat. Commun.* **2017**, *8*, 15119.
- [36] L. Zhao, D. H. Torchinsky, H. Chu, V. Ivanov, R. Lifshitz, R. Flint, T. Qi, G. Cao, D. Hsieh, *Nat. Phys.* **2016**, *12*, 32.
- [37] H. Murayama, K. Ishida, R. Kurihara, T. Ono, Y. Sato, Y. Kasahara, H. Watanabe, Y. Yanase, G. Cao, Y. Mizukami, T. Shibauchi, Y. Matsuda, S. Kasahara, *Phys. Rev. X* **2021**, *11*, 011021.
- [38] X. Teng, L. Chen, F. Ye, E. Rosenberg, Z. Liu, J.-X. Yin, Y.-X. Jiang, J. S. Oh, M. Z. Hasan, K. J. Neubauer, B. Gao, Y. Xie, M. Hashimoto, D. Lu, C. Jozwiak, A. Bostwick, E. Rotenberg, R. J. Birgeneau, J.-H. Chu, M. Yi, P. Dai, *Nature* **2022**, *609*, 490.
- [39] Y.-X. Jiang, J.-X. Yin, M. M. Denner, N. Shumiya, B. R. Ortiz, G. Xu, Z. Guguchia, J. He, M. S. Hossain, X. Liu, J. Ruff, L. Kautzsch, S. S. Zhang, G. Chang, I. Belopolski, Q. Zhang, T. A. Cochran, D. Multer, M. Litskevich, Z.-J. Cheng, X. P. Yang, Z. Wang, R. Thomale, T. Neupert, S. D. Wilson, M. Z. Hasan, *Nat. Mater.* **2021**, *20*, 1353.
- [40] X. Feng, K. Jiang, Z. Wang, J. Hu, *Sci. Bull.* **2021**, *66*, 1384.
- [41] A. F. May, Y. Liu, S. Calder, D. S. Parker, T. Pandey, E. Cakmak, H. Cao, J. Yan, M. A. McGuire, *Phys. Rev. B* **2017**, *95*, 174440.
- [42] Y. Zhang, X. Jin, Z. Li, K. Yang, L. Wei, X. Mi, A. Wang, X. Zhou, X. Yang, Y. Chai, M. He, *Phys. Rev. B* **2025**, *112*, L081109.
- [43] Y. Liu, C. Petrovic, *Phys. Rev. B* **2018**, *98*, 064423.
- [44] L. Onsager, *Phys. Rev. J. Arch.* **1944**, *65*, 117.
- [45] Y. Liu, Z. Hu, M. Abeykoon, E. Stavitski, K. Attenkofer, E. D. Bauer, C. Petrovic, *Phys. Rev. B* **2021**, *103*, 245122.
- [46] S. Li, H.-Z. Lu, X. C. Xie, *Phys. Rev. B* **2023**, *107*, 235202.
- [47] G. D. Mahan, *Many-Particle Physics*, 3rd ed., Kluwer Academic/Plenum Publishers, New York **2000**.
- [48] J. Fang, J. Hu, X. Chen, Y. Liu, Z. Yin, Z. Ying, Y. Wang, Z. Wang, Z. Li, S. Zhu, Y. Xu, S. T. Pantelides, H.-J. Gao, *Phys. Rev. Lett.* **2025**, *134*, 256302.
- [49] S. W. Lovesey, *Phys. Rev. B* **2023**, *107*, 224410.
- [50] G. Sala, J. Y. Y. Lin, A. M. Samarakoon, D. S. Parker, A. F. May, M. B. Stone, *Phys. Rev. B* **2022**, *105*, 214405.
- [51] M. Wang, C. Andrews, S. Reimers, O. J. Amin, P. Wadley, R. P. Champion, S. F. Poole, J. Felton, K. W. Edmonds, B. L. Gallagher, A. W. Rushforth, O. Makarovskiy, K. Gas, M. Sawicki, D. Kriegner, J. Zubac, K. Olejnik, V. Novák, T. Jungwirth, M. Shahrokhtvand, U. Zeitler, S. S. Dhesi, F. Maccherozzi, *Phys. Rev. B* **2020**, *101*, 094429.
- [52] Y. Dai, Y. W. Zhao, L. Ma, M. Tang, X. P. Qiu, Y. Liu, Z. Yuan, S. M. Zhou, *Phys. Rev. Lett.* **2022**, *128*, 247202.
- [53] D. Tu, C. Wang, J. Zhou, *Phys. Rev. B* **2025**, *112*, L041405.
- [54] Y. Yahagi, D. Miura, A. Sakuma, *J. Phys. Soc. Jpn.* **2020**, *89*, 044714.